Smart Materials and Structures

PAPER

Development of a deflector-jet electrohydraulic servovalve using a giant magnetostrictive material

IOP Publishing Smart Materials and Structures
Smart Mater. Struct. 23 (2014) 115001 (19pp) doi:10.1088/0964-1726/23/11/115001

Development of a deflector-jet electrohydraulic servovalve using a giant magnetostrictive material

Yuchuan Zhu and Yuesong Li

College of Mechanical and Electrical Engineering, Nanjing University of Aeronautics and Astronautics, Nanjing 210016, People's Republic of China

E-mail: meeyczhu@nuaa.edu.cn

Received 27 March 2014, revised 23 July 2014
Accepted for publication 15 August 2014
Published 19 September 2014

Abstract

Giant magnetostrictive actuators (GMAs) have received considerable attention in recent years and are becoming increasingly important in the exploitation of a new type electrohydraulic servovalve. In this paper, a deflector-jet servovalve (DJSV) using a giant magnetostrictive material (GMM) is developed for the first time, and the servovalve is mechanically less complex than a conventional DJSV. Next, a mathematical model of the GMM-based DJSV is built, which involves five submodels: a dynamic model of the power amplifier; a dynamic magnetization model of the GMM rod; a magnetoelastic model of the GMM rod; a kinetic model of the GMA; and a deflector-jet amplifier model. The experimental platform used for measuring the performance of the GMM-based DJSV is established, the prototype valve is fabricated, and the related unknown parameters are identified by experimental data from the GMA. Finally, a simulation and experimental research are performed on the GMM-based DJSV; the results indicate that the present GMM-based DJSV has a large output-pressure range, a rapid response, and a high bandwidth, which provides a competitive way to develop a new type of high-frequency and high-flow-rate electrohydraulic servovalve. Additionally, the measured characteristics of the prototype valve are in good agreement with the predicted results and demonstrate that the operational concept is viable, and the present mathematical model is reliable.

Keywords: giant magnetostrictive actuator, servovalve, frequence width, deflector-jet, dynamic models

1. Introduction

Servovalves are compact, accurate, high-bandwidth modulating valves widely used in aeromechanics and industrial defense applications in which high power and rapid response are required. The servovalves can transform a changing analog or digital input signal into a stepless hydraulic output (flow or pressure) and may be single-stage or two-stage devices. The first stage of such valves has assumed a variety of forms, including a sliding spool, a flapper-nozzle, a jet-pipe, and a deflector-jet, whose performance characteristics are shown in table 1.

A double-nozzle flapper is a full bridge with two variable arms, and the use of two nozzles makes the design relatively immune to changes in its null or zero differential pressure position and/or temperature. A jet-pipe servovalve is a full bridge, four-variable arm configuration similar to the underlapped four-way spool valve that has a 'single inlet' first stage, making it a fail-to-center design. There is no risk of unbalance from contamination because there is only a single source of fluid for the first stage, and it may be less sensitive to the effects of contamination than flapper-nozzle valves are. In other words, the main advantage of jet-pipe servovalves is their insensitivity to dirty fluids. However, the jet-pipe servovalve is not as widely used as the flapper-valve servovalve in the two-stage servovalve because of its large null flow, unpredictable characteristics, and slower response. A modification in the jet-pipe servovalve results in a new design,

Table 1. Performance characteristics of flapper-nozzle, jet-pipe, and deflector-jet.

Design/Performance characteristic	Flapper-Nozzle	Jet-Pipe	Deflector-Jet
Orifice size	Very small	Relatively large	Relatively large
Contamination sensitivity	Very sensitive	More tolerant	More tolerant
Potential for 'noisy' operation	Low	Low	High
Failure mode (plugged orifice)	Hard over	Passive	Passive
Pressure and flow recovery	Jet-pipe and deflector-jet are more than twice that of the flapper nozzle		
Low temperature performance	Good at lower pressures	Good	Inferior
Pressure feedback	Present causing instability	None	None
Sensitivity to erosion	High	Low	Low

known as the deflector-jet servovalve (DJSV); the design aspects and the operating principle of a DJSV are elaborated in Moog technical bulletin 121.

The present designs of pilot-operated servovalves are either of a flapper-nozzle type or of a jet-pipe type, and the design aspects and various configurations of servovalves, particularly flapper-nozzle types, are available in many textbooks (Merrit 1967, Watton 1989, McCloy and Martin 1980). However, studies investigating deflector-jet type servovalves are notably scarce.

Giant magnetostrictive materials (GMMs) are a new type of functional material appearing in recent years with, for instance, giant strain, fast response speed, high energy density, and a large output force (Grunwald and Olabi 2008, Olabi and Grunwald 2008, Pradhan 2005, Shang *et al* 2008, Sun and Zheng 2006, Valadkhan *et al* 2010, Zheng *et al* 2007, Zhou *et al* 2006). Magnetostriction is the property that causes certain ferromagnetic materials to change shape in a magnetic field. When a magnetic field is applied, magnetic domains in the crystal rotate, providing proportional, positive, and repeatable expansion in microseconds. Using GMM to design a new type of actuator that can replace traditional actuators such as torque motors or force motors will enhance the response speed and precision of servovalves (Urai and Tanaka 2001, Karunanidhi and Singaperumal 2010, Ding *et al* 2002, Wang *et al* 2005, 2006, 2007).

Giant magnetostrictive actuators (GMAs) have received considerable attention in recent years and are becoming increasingly important in the exploitation of new types of electromechanical devices (Karunanidhi and Sigaperumal (2010), Li *et al* 2011a, Braghin *et al* 2012), which can be used to drive the spool valve directly (Hiratsuka and Urai 1994). In 1994, a direct-drive servovalve using a giant magnetostrictive material was developed and showed a high performance (i.e., high output power, fast response, and a high resistance to environmental factors such as humidity). The valve does not have first-stage flow and is not influenced by contamination. The valve's rated flow is 2 L min^{-1}, its step response with rising time is approximately 1 ms, and it has a 630 Hz amplitude-frequency width (–3 dB) and a 450 Hz phase-frequency width (–90°). In 1995, a direct-drive servovalve using a giant magnetostrictive actuator with a stroke-expansion system was developed using Pascal's theory (Urai 1995). This system had a rated flow of 6 L min^{-1}, a step response with rising time of approximately 1 ms, a 250 Hz amplitude-frequency width (−3 dB), and a 180 Hz phase-frequency width (−90°). In 2001, a servovalve (Urai and Tanaka 2001) was presented using a giant magnetostrictive tandem actuator with a 250 Hz frequency width (–3 dB) and a 50 L min^{-1} flow rate. In 2005, a pneumatic and hydraulic single-nozzle flapper-type servovalve based on a GMA was systematically and thoroughly analyzed and researched (Ding *et al* 2002, Wang *et al* 2005, 2006, 2007). The structure and principles of a pneumatic servovalve with GMMs are presented. An experimental study is performed, and the experimental results indicate that the GMM pneumatic servovalve has wide pressure-control properties, good linearity, and a high response speed. The hydraulic GMA nozzle-flapper servovalve has wide pressure-control properties that perform up to 0.52 MPa, good linearity that is approximately 2.5%, a fast response speed with a rise time less than 1 ms, and a 680 Hz frequency width (−3 dB). The research results show that the flapper structure driven directly by the GMA is simple, reliable, and controllable, and the pressure-control performance is improved by adopting a temperature-compensation mechanism with prepressure exerted organization. In 2010 and 2011, Wang focused on a seawater hydraulic servovalve driven by a diphase opposition giant magnetostrictive self-sensing actuator and servovalve (Wang *et al* 2009, 2010), which achieved dynamic real-time control with a microprocessor. In 2010, a magnetostrictive actuator with a flexure amplifier and a magnetically biased magnetostrictive actuator was designed, built, and integrated into an existing flapper-nozzle servovalve (replacing the torque motor) by Karunanidhi and Singaperumal (Karunanidhi and Singaperumal 2010). From the experimental results, it is evident that the valve step response of 7.8 ms driven by the giant magnetostrictive actuator is faster than that of a conventional torque motor (11.2 ms) and that the valve flow rate of 8.0 L min^{-1} is larger than that of a conventional torque motor (7.6 L min^{-1}). The results show that the valve has satisfactory static and dynamic characteristics for applications in high-speed actuation systems. In 2013, a novel closed-loop piezohydraulic servovalve design was investigated (Sangiah *et al* 2013). Its design and performance are suitable for safety-critical aerospace applications, particularly primary flight control. The bimorph deflects a jet of fluid to create a pressure differential across the valve spool. The measured

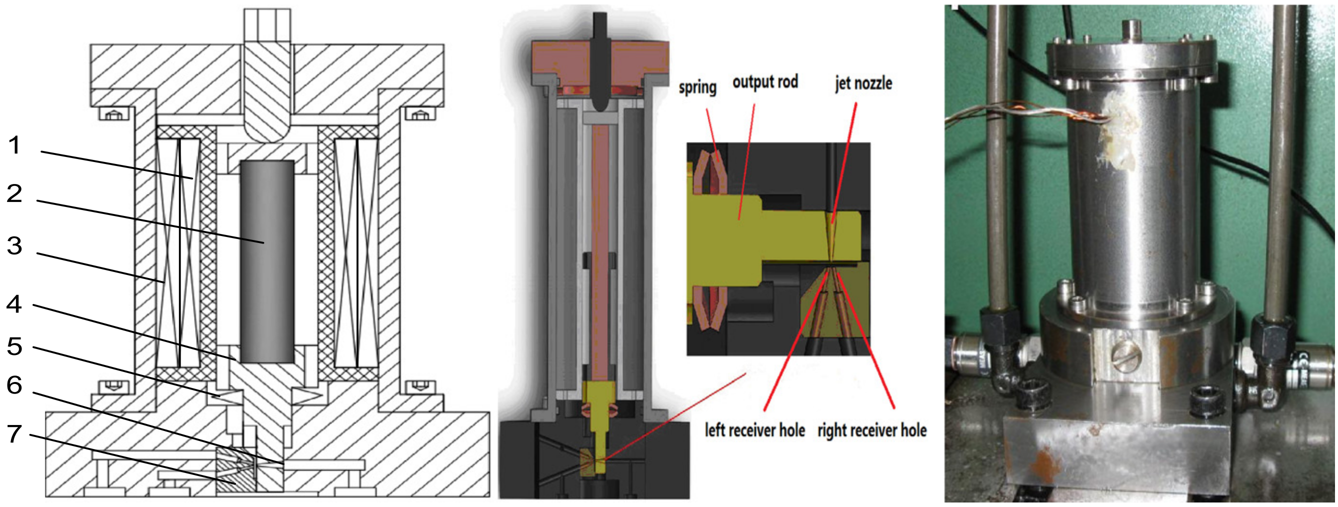

1. Driving solenoid coil 2.GMM rod 3. Biased solenoid coil 4. Output rod 5. Spring 6. Deflector pole 7. Receiver

(a) Structural schematic diagram (b) Principled sample machine

Figure 1. Configuration of a GMM-based DJSV.

characteristics of the prototype valve are in good agreement with the simulated results, and prove that the operational concept is viable.

However, no detailed design approaches and model of deflector-jet-type servovalves have been reported so far, and this is especially the case for GMM-based DJSVs. Furthermore, due to the conventional drive mode of deflector-jet servovalves, the lower resolution and narrower working bandwidth confine the applications of the deflector-jet servovalve. Hence, developing a new type of electrohydraulic servovalve that has more ideal characteristics will have an important practical impact. In this paper, a novel deflector-jet servovalve concept called a GMM-based DJSV is investigated, which will potentially have a faster response. In particular, for the first time, a GMA is developed to move a jet-nozzle in a deflector-jet-type servovalve. This means that the conventional electromagnetic torque motor is replaced by a GMA in this novel deflector-jet servovalve. Its detailed design, considering several parameters, is presented. Further simulation and experimental results are also included.

2. Valve description

As shown in figure 1, a deflector-jet electrohydraulic servovalve consists of a GMA and a deflector-jet hydraulic amplifier. The GMA includes a biased solenoid coil used for providing a biased magnetic field, a driving solenoid coil generating a control magnetic field, a GMM rod, an output rod, a spring used for applying prestress onto the GMM rod to obtain a larger magnetostrictive strain with the same magnetic field, and a screw that can be adjusted to vary the prestress according to the demand. The thermal deformation-compensating module (shell) can balance the thermal deformation generated by the GMM rod.

When the biased solenoid coil and the driving solenoid coil are switched on, the fluid flow between the GMM rod and the skeleton can cool the GMM rod, which contributes to improved jet-nozzle movement accuracy. When the sign of the magnetic field produced by the driving solenoid coil is identical to the sign of the bias magnetic field, the GMM rod elongates. If the sign of the magnetic field produced by the driving solenoid coil is the opposite of the sign of the biased magnetic field, the GMM rod is shorter than in the initial condition.

As shown in figure 1(a), the driving coil wound around the GMM rod acts as the excited magnetic field, which causes the GMM rod to expand in the magnetic field direction. This provides a force to the deflector pole (output rod, as shown in figure 1(a)) and accordingly results in the movements of the deflector pole. Simultaneously, the supply-pressure oil produces a jet that divides equally between the two receivers; in a GMM-based DJSV, the pressure energy of the fluid is converted into kinetic energy at the jet-nozzle exit and is then reconverted as pressure energy into the receiver holes. Oil under high pressure flows out of the jet-nozzle exit and impinges on a receiver hole. Two small-diameter receiver holes located side-by-side on the receiver are connected to either end of the load. With the jet-pipe centered over the two holes, equal pressures are developed on each side of the load. When the GMM rod causes the jet-nozzle to move off-center, the jet impinges more on one hole than the other. This creates a pressure imbalance across the load. When the nozzle is centered between the two receiver holes, the pressure difference between the two receiver holes is zero. However, when the nozzle is moved toward one of the receiver holes by the GMM rod, the pressure at this receiver hole is greater than at the other receiver hole, thus displacing the spool position.

3. Valve model

The energy-conversion process in a GMM-based DJSV involves five stages: the stage from the input voltage to the

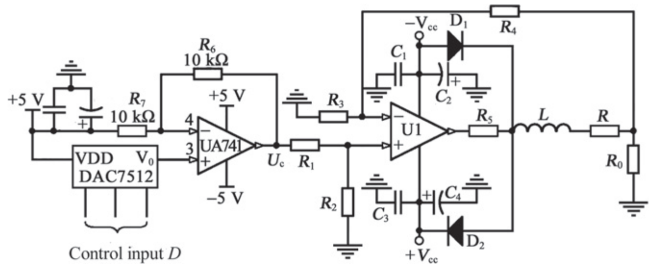

Figure 2. Circuit diagram of a power amplifier.

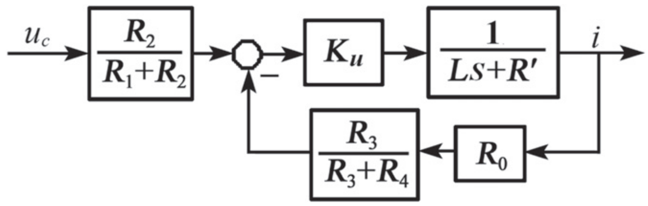

Figure 3. Transfer function block diagram of a power amplifier.

applied current of the drive coil; the stage from the electrical energy to the magnetic energy; the stage from magnetic energy to the elastic potential energy; the stage from the elastic potential energy to the mechanical energy; and the stage from the mechanical energy to the fluid pressure energy. In the first four stages, electrical-mechanical energy transformation is achieved, and the last stage achieves mechanical-hydraulic energy amplification. Thus, the model of a GMM-based DJSV involves five submodels from the viewpoint of energy conversion: the dynamic model of the power amplifier; the dynamic magnetization model that describes the relationship between the exciting current and the magnetization of the GMM rod; the magnetoelastic model describing the relationship between the magnetostrictive strain and the magnetization of GMM rod; the kinetic model of the GMA describing the relationship between the deflector pole displacement (magnetostrictive displacement) and the magnetostrictive strain; and the deflector-jet amplifier model between the deflector pole displacement and the net pressure difference from the two receivers.

3.1. Dynamic model of the power amplifier

The drive coil is an inductance element that makes the input current lag behind the input voltage. Thus, to obtain a fast current response, we designed a power amplifier with an integrated power amplifier by depth electric current negative feedback technology, which can eliminate the input current lag. Its circuit diagram and transfer function block diagram are shown in figures 2 and 3, respectively.

The transfer function of the power amplifier can be written as follows, according to figure 3:

$$i = \frac{R_2}{R_1 + R_2}\frac{K_u}{Ls + R + R_5}\frac{u_c}{1 + \dfrac{K_u}{Ls + R + R_5}\dfrac{R_3 R_0}{R_3 + R_4}}. \quad (1)$$

Taking $R_1 = R_2$ and $R_3 = R_4$, equation (1) can be rewritten as follows:

$$i = \frac{K_u}{Ls + R + R_5}\frac{u_c}{2\left(1 + \dfrac{K_u}{Ls + R + R_5}\dfrac{R_0}{2}\right)} = \frac{K_u u_c}{2Ls + \left(2R + 2R_5 + K_u R_0\right)}, \quad (2)$$

where K_u is the open-loop gain of the integrated operational amplifier, u_c is the input voltage, L is the inductance of the drive coil, and R and R_0 are the resistance of the drive coil and the sampling resistance, respectively.

3.2. Magnetization model of the GMM rod

In the above-mentioned configuration of the GMM-based DJSV, the energy equation is given as follows in the magnetization process of the GMM rod:

$$P_{\rm in} = P_{\rm m} + P_{\rm h} + P_{\rm eddy} + P_{\rm ex}, \quad (3)$$

where $P_{\rm in}$ and $P_{\rm m}$ represent the energy input and the magnetostatic energy, respectively, and $P_{\rm h}$, $P_{\rm eddy}$, and $P_{\rm ex}$ represent the energy losses from magnetic hysteresis, the eddy current, and the excess, respectively.

For low magnetic fields, the magnetization process of the GMM rod obeys Rayleigh's law. The magnetic hysteresis power loss is given by

$$P_{\rm h} = \int_V \frac{4}{3}\mu_0 \eta_0 H_{\rm m}^3 f \, {\rm d}V = K'_{\rm h} H_{\rm m}^3 f V, \quad (4)$$

where η_0 is the Rayleigh constant, V is the volume of the GMM rod, $K'_{\rm h}$ is the hysteresis-loss coefficient at low fields, and f is the frequency of the applied magnetic field.

Due to the existence of the permanent magnet, although the applied magnetic field generated by the alternating current may not be high, the total magnetic field is intermediate, and irreversible domain rotation occurs as the domain magnetization rotates between the magnetically easy axes. Based on results obtained by experiments with various ferromagnetic materials with sinusoidal currents, Charles Steimetz proposed an empirical formula for calculating hysteresis loss analytically. The magnetic hysteresis power loss, $P_{\rm h}$, is provided by Steinmetz's empirical formula,

$$P_{\rm h} \approx \int_V K_{\rm h} B_{\rm m}^n f \, {\rm d}V = K_{\rm h} B_{\rm m}^n f V, \quad (5)$$

where $K_{\rm h}$ is the hysteresis loss coefficient at intermediate fields and n is the Steinmetz exponent that varies from 1.5 to 2.5.

To reduce the classical eddy-current losses in a sinusoidal magnetic field, the GMM rod applied in a deflector-jet electrohydraulic servovalve is made in the form of laminations. The eddy-current loss is calculated as follows

(Jiles 1994):

$$P_{\mathrm{eddy}} = \int_V \frac{d_1^2}{2\rho\beta}\left(\frac{\mathrm{d}B_\mathrm{c}}{\mathrm{d}t}\right)^2 \mathrm{d}V, \tag{6}$$

where ρ and d_1 are the electrical resistivity and the thickness of the lamination of the GMM rod, respectively.

Equation (6) is derived on the condition that the magnetic flux density on the cross section of the GMM rod is distributed evenly and the laminations are rectangular in shape. Equation (6) must be rearranged as follows:

$$\begin{aligned} P_{\mathrm{eddy}} &= \int_V \frac{1}{T}\int_0^T \frac{d_1^2}{2\rho\beta}\left(\frac{\mathrm{d}B_\mathrm{c}}{\mathrm{d}t}\right)^2 \mathrm{d}t\mathrm{d}V \\ &= \int_V \frac{1}{T}\int_0^T \frac{K_\mathrm{e}}{2\pi^2}\left(\frac{\mathrm{d}B_\mathrm{c}}{\mathrm{d}t}\right)^2 \mathrm{d}t\mathrm{d}V \\ &= K_\mathrm{e}\left(B_\mathrm{m}f\right)^2 V, \end{aligned} \tag{7}$$

where K_e is the eddy-current loss coefficient, $K_\mathrm{e} = \frac{\pi^2 d_1^2}{\rho\beta}$, and T is the period.

In a sinusoidal magnetic field, the excess loss that results from changes in the domain configuration also must be considered, and this component of the loss can be expressed as (Jiles 1994)

$$P_{\mathrm{ex}} = \int_V \sqrt{\frac{G_0 d_1 w H_0}{\rho}}\left(\frac{\mathrm{d}B_\mathrm{c}}{\mathrm{d}t}\right)^{1.5} \mathrm{d}V, \tag{8}$$

where w is the width of the laminations, H_0 is a parameter representing the internal potential experienced by the domain walls, and G_0 is a dimensionless constant of the valve, 0.1356.

Under the restricted condition of B varying sinusoidally with time, the excess loss can be calculated as

$$\begin{aligned} P_{\mathrm{ex}} &= \int_V \frac{1}{T}\int_0^T \sqrt{\frac{G_0 d_1 w H_0}{\rho}}\left(\frac{\mathrm{d}B_\mathrm{c}}{\mathrm{d}t}\right)^{1.5} \mathrm{d}t\mathrm{d}V \\ &= K_{\mathrm{ex}}\left(B_\mathrm{m}f\right)^{1.5} V, \end{aligned} \tag{9}$$

where K_{ex} is the excess-loss coefficient, $K_{\mathrm{ex}} = 8.67\sqrt{\frac{G_0 d_1 w H_0}{\rho}}$.

Thus, the total magnetic energy loss can be written as

$$P_{\mathrm{loss}} = P_\mathrm{h} + \left[K_\mathrm{e}\left(B_\mathrm{m}f\right)^2 + K_{\mathrm{ex}}\left(B_\mathrm{m}f\right)^{1.5}\right]V. \tag{10}$$

The magnetic energy loss can also be expressed as

$$P_{\mathrm{loss}} = V\frac{1}{T}\oint H_\mathrm{c}\mathrm{d}B_\mathrm{c} = \pi f \mu_0 \mu'' H_\mathrm{m}^2 V. \tag{11}$$

The imaginary part of the complex relative permeability can be calculated as follows:

$$\mu'' = \frac{P_{loss}}{\pi f \mu_0 H_\mathrm{m}^2 V}. \tag{12}$$

Thus, at low magnetic fields

$$\mu'' = \frac{K_\mathrm{h}' H_\mathrm{m}^3 + K_\mathrm{e} B_\mathrm{m}^2 f + K_{\mathrm{ex}} B_\mathrm{m}^{1.5} f^{0.5}}{\pi \mu_0 H_\mathrm{m}^2}. \tag{13}$$

At intermediate magnetic fields

$$\mu'' = \frac{K_\mathrm{h} B_\mathrm{m}^\mathrm{n} + K_\mathrm{e} B_\mathrm{m}^2 f + K_{\mathrm{ex}} B_\mathrm{m}^{1.5} f^{0.5}}{\pi \mu_0 H_\mathrm{m}^2}. \tag{14}$$

In a closed magnetic circuit, the applied magnetic field, H_c, generated by alternating current i is given by

$$H_\mathrm{c} = \frac{Ni}{k_\mathrm{f} L} = \frac{NI_\mathrm{m}}{k_\mathrm{f} L}\cos\omega t = H_\mathrm{m}\cos\omega t. \tag{15}$$

The complex number form of the applied magnetic field is written as (Engdahl 1999)

$$H_\mathrm{c} = H_\mathrm{m} e^{j\omega t}, \tag{16}$$

where N is the number of the excitation coil turns, I_m is the amplitude of the alternating current, k_f is the leakage coefficient of the magnetic flux, L is the length of the GMM rod, H_m is the amplitude of the applied magnetic field, and ω is the angular frequency.

In a sinusoidal magnetic field, the relative permeability of the GMM rod is a complex number, and the complex number form of magnetic flux density is given by

$$B_\mathrm{c} = \mu_0(\mu' - j\mu'')\dot{H}_\mathrm{c} = \mu_0 H_\mathrm{m}\left[\mu' e^{j\omega t} + \mu'' e^{j(\omega t - \pi/2)}\right]. \tag{17}$$

Therefore, based on equation (15), the magnetic flux density, B_c, in the GMM rod can be written as

$$\begin{aligned} B_\mathrm{c} &= \mu_0\mu' H_\mathrm{m}\cos\omega t + \mu_0\mu'' H_\mathrm{m}\cos\left(\omega t - \frac{\pi}{2}\right) \\ &= \mu_0 H_\mathrm{c}(\mu' + \mu''\ \tan\omega t). \end{aligned} \tag{18}$$

Equation (18) can be rewritten as

$$\begin{aligned} B_\mathrm{c} &= \mu_0\mu' H_\mathrm{m}\cos\omega t + \mu_0\mu'' H_\mathrm{m}\sin\omega t \\ &= \mu_0\sqrt{\mu'^2 + \mu''^2} H_\mathrm{m}\cos(\omega t - \varphi), \end{aligned} \tag{19}$$

where φ is the lag angle, and its value can be calculated as

$$\varphi = \arctan\left(\frac{\mu''}{\mu'}\right). \tag{20}$$

The amplitude of the magnetic flux density can be obtained from equation (17):

$$B_\mathrm{m} = \mu_0\sqrt{\mu'^2 + \mu''^2} H_\mathrm{m}. \tag{21}$$

Therefore, the real part of the complex relative permeability can be calculated as

$$\mu' = \sqrt{\left(\frac{B_\mathrm{m}}{\mu_0 H_\mathrm{m}}\right)^2 - \mu''^2}. \tag{22}$$

Equations (14) and (22) show that B_m is the key parameter to calculate the complex permeability of the GMM rod. To obtain the amplitude of the magnetic flux density when the giant magnetostrictive actuator is driven, a sensing coil is wound around the excitation coil.

The voltage of the induction coil is given by

$$E = -N_c A_c \frac{dB}{dt}, \tag{23}$$

where N_c is the number of sensing coil turns and A_c is the cross-sectional area of induction coil.

Due to the sinusoidal variation of the magnetic flux density with time, the amplitude of the magnetic flux density can be obtained from equation (23),

$$B_m = \frac{E_m}{\omega N_c A_c}, \tag{24}$$

where E_m is the amplitude of the induced voltage.

The applied magnetic field, H, consists of the biased magnetic field, H_b, and the control magnetic field, H_c; generally, the biased magnetic field, H_b, is constant, and the control magnetic field, H_c, can be generated by a step-applied current or a sinusoidal applied current.

First, if the control magnetic field, H_c, is generated by a step-applied current, and the value of the control magnetic field, H_c, is far less than that of the bias magnetic field, H_b, then the module of the GMM rod relative to the permeability can be treated as a constant. The energy equation is provided as follows in the dynamic magnetization process of the GMM rod:

$$P_{in} = P_m + P_{eddy} + P_{ex}. \tag{25}$$

Substituting equations (7) and (9) into (25) yields

$$\mu_0 \int (\mu_r - 1) H_c dH_c = \mu_0 \int M_c dH_c + \int \frac{K_e}{2\pi^2}\left(\frac{dB_c}{dt}\right)^2 dt + \int \frac{K_{ex}}{8.67}\left(\frac{dB_c}{dt}\right)^{1.5} dt. \tag{26}$$

Differentiating equation (26) by the variable H_c leads to

$$\mu_0(\mu_r - 1)H_c = \mu_0 M_c + \frac{K_e}{2\pi^2}\frac{dB_c}{dt}\frac{dB_c}{dH_c} + \frac{K_{ex}}{8.67}\left(\frac{dB_c}{dt}\right)^{0.5}\frac{dB_c}{dH_c}. \tag{27}$$

Replacing $\frac{dB_c}{dH_c}$ by $\mu_0\mu_r$ and dividing by μ_0 gives

$$(\mu_r - 1)H_c = M + \frac{\mu_r K_e}{2\pi^2}\frac{dB_c}{dt} + \frac{K_{ex}\mu_r}{8.67}\left(\frac{dB_c}{dt}\right)^{0.5}. \tag{28}$$

Replacing $\frac{dB_c}{dH_c}$ by $\frac{dM_c}{dH_c}$ gives

$$(\mu_r - 1)H_c = M_c + \frac{\mu_r K_e}{2\pi^2}\frac{dM_c}{dt} + \frac{K_{ex}\mu_r}{8.67}\left(\frac{dM_c}{dt}\right)^{0.5}. \tag{29}$$

If K_e and K_{ex} are identified (they can be obtained from equation (14)), then the magnetization, M_c, can be solved numerically by using the Newton–Raphson method.

Second, if the control magnetic field, H_c, is generated by a sinusoidal applied current, then the magnetization, M_c, can be deduced from the magnetic flux density, B_c, and the applied magnetic field, H_c:

$$M_c = \frac{B_c}{\mu_0} - H_c = H_c(\mu' - 1 + \mu'' \tan \omega t). \tag{30}$$

Considering the relative permeability, $\mu_r = \mu' - j\mu''$, then

$$\mu' = \sqrt{|\mu_r|^2 - (\mu'')^2}. \tag{31}$$

Substituting (15) and (31) into (30) yields

$$M_c = H_m\left(\left(\sqrt{|\mu_r|^2 - (\mu'')^2} - 1\right)\cos \omega t + \mu'' \sin \omega t\right). \tag{32}$$

Rewriting equation (32) yields

$$M_c = \sqrt{\left(\sqrt{|\mu_r|^2 - (\mu''_h)^2} - 1\right)^2 + (\mu'')^2} \times H_m \cos(\omega t - \theta_h), \tag{33}$$

where θ_h is the lag angle caused by the hysteresis

$$\theta_h = \arctan\left(\frac{\mu''}{\sqrt{|\mu_r|^2 - (\mu'')^2} - 1}\right). \tag{34}$$

Equations (33) and (34) are only valid for a low-frequency sinusoidal magnetic field to a high frequency sinusoidal magnetic field. In this case, we can acquire the GMM rod practical magnetic field distribution according to Maxwell's equation, and the applied magnetic field, H_c, yields

$$\frac{d^2H_c}{dr^2} + \frac{1}{r}\frac{dH_c}{dr} = j\omega\gamma\mu H_c, \tag{35}$$

considering the boundary conditions

$$H_c(r_G, t) = H_m e^{j\omega t}. \tag{36}$$

Thus, the solution of equation (35) is

$$H_c(r, t) = \frac{J_0\left(r\sqrt{-j\omega\gamma\mu}\right)}{J_0\left(r_G\sqrt{-j\omega\gamma\mu}\right)} H_m e^{j\omega t}, \tag{37}$$

where $J_0(\cdot)$ is a zero-order Bessel function.

In the GMM rod axes,

$$H_c(0, t) = \frac{J_0(0)}{J_0\left(r_G\sqrt{-j\omega\gamma\mu}\right)} H_m e^{j\omega t} = \frac{1}{J_0\left(r_G\sqrt{-j\omega\gamma\mu}\right)} H_m e^{j\omega t}. \tag{38}$$

The GMM rod practical magnetic field distribution

$$H_c = \frac{\mathrm{ber}\left(r_G\sqrt{\omega\gamma\mu}\right) - j\mathrm{bei}\left(r_G\sqrt{\omega\gamma\mu}\right)}{\mathrm{ber}^2\left(r_G\sqrt{\omega\gamma\mu}\right) + \mathrm{bei}^2\left(r_G\sqrt{\omega\gamma\mu}\right)} H_m e^{j\omega t}. \tag{39}$$

Rewriting equation (39) gives

$$H_c = \frac{1}{\sqrt{\mathrm{ber}^2\left(r_G\sqrt{\omega\gamma\mu}\right) + \mathrm{bei}^2\left(r_G\sqrt{\omega\gamma\mu}\right)}} \times H_m \cos\left(\omega t - \theta_e\right), \tag{40}$$

where θ_e is the lag angle caused by the eddy,

$$\theta_e = \arctan\left(\frac{\mathrm{bei}\left(r_G\sqrt{\omega\gamma\mu}\right)}{\mathrm{ber}\left(r_G\sqrt{\omega\gamma\mu}\right)}\right). \tag{41}$$

Considering equations (33) and (34), it is possible to rewrite equation (40) to give

$$M_c = \sqrt{\frac{\left(\sqrt{\left|\mu_r\right|^2 - (\mu'')^2} - 1\right)^2 + (\mu'')^2}{\mathrm{ber}^2\left(r_G\sqrt{\omega\gamma\mu}\right) + \mathrm{bei}^2\left(r_G\sqrt{\omega\gamma\mu}\right)}} \times H_m \cos\left(\omega t - \theta_h - \theta_e\right). \tag{42}$$

3.3. Magnetomechanical model of GMM rod

According to the discussion in reference (Li and Zhu 2012b), the free strain due to magnetostriction along field direction λ is given by

$$\lambda = \frac{3}{2}\frac{\lambda_S}{M_S^2}M^2, \tag{43}$$

where λ_S and M_S are the saturation magnetostriction and the saturation magnetization, respectively.

Considering that the actual magnetic field is caused by the biased magnetic field and the control magnetic field, the practical magnetostrictive λ yields

$$\lambda = \frac{3}{2}\frac{\lambda_S}{M_S^2}\mathrm{M}^2\left(H_c + H_b\right) - \frac{3}{2}\frac{\lambda_S}{M_S^2}M_b^2 = k_\lambda\left[\mathrm{M}^2\left(H_c + H_b\right) - M_b^2\right], \tag{44}$$

where H_b is the biased magnetic field in the GMM rod, M_b is the biased magnetization intensity in the GMM rod, and k_λ is a constant,

$$k_\lambda = \frac{3}{2}\frac{\lambda_S}{M_S^2} \tag{45}$$

The output displacement, y, of a giant magnetostrictive actuator can be written as follows according to Hooke's law:

$$\frac{Ky}{A_G} = E^H\lambda, \tag{46}$$

where K is equivalent to the stiffness of the GMM rod and A_G, E^H are the cross-sectional area and the elastic modulus of the GMM rod, respectively.

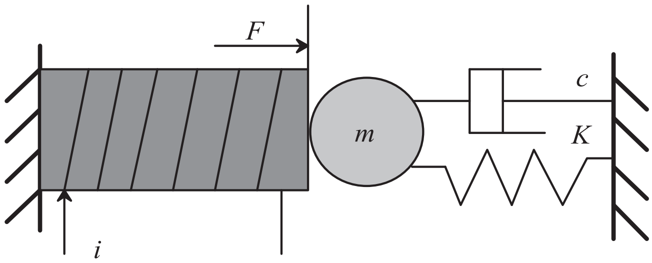

Figure 4. Lumped parameter model of giant magnetostrictive actuator.

Substituting (44) into (46) yields

$$y = \frac{E^H A_G \lambda}{K} = k_\lambda \frac{E^H A_G}{K}\left[\mathrm{M}^2\left(H_c + H_b\right) - M_b^2\right]. \tag{47}$$

If an experimental point (H_0, y_0) is known,

$$y_0 = k_\lambda \frac{E^H A_G}{K}\left(M_0^2 - M_b^2\right) = \frac{k_\lambda E^H A_G\left(\left|\mu_r\right| - 1\right)^2}{K}\left[\left(H_0 + H_b\right)^2 - H_b^2\right]. \tag{48}$$

Substituting (48) into (47) yields

$$y = \frac{\mathrm{M}^2\left(H_c + H_b\right) - \left(\left|\mu_r\right| - 1\right)^2 H_b^2}{\left(\left|\mu_r\right| - 1\right)^2\left[\left(H_0 + H_b\right)^2 - H_b^2\right]} y_0. \tag{49}$$

3.4. Kinetic model of a giant magnetostrictive actuator

The lumped parameter model of giant magnetostrictive actuator is a mass-spring-damping system (Tan and Baras 2004), as shown in figure 4.

Magnetostrictive energy in the GMM rod can be written by

$$W_\lambda = \frac{E^H}{2}\int \lambda^2 dV = \frac{E^H \lambda^2}{2} A_G L_G. \tag{50}$$

Based on the conservation law of mechanical energy, we can obtain

$$W_\lambda = \frac{1}{2}mv^2 + C\int v^2 dt + \frac{1}{2}Ky^2, \tag{51}$$

where v are the velocity of the giant magnetostrictive actuator. m, C, K are the equivalent mass, equivalent damping, and equivalent stiffness of giant magnetostrictive actuator, respectively.

Substituting (50) into (51), and then differentiating equation (51) leads to

$$E^H A_G \lambda \frac{d\lambda}{dt} L_G = mv\frac{dv}{dt} + Cv^2 + Kyv. \tag{53}$$

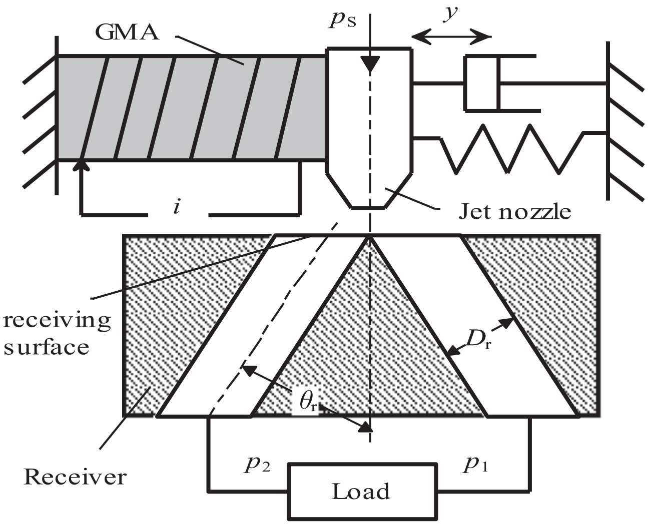

Figure 5. Schematic representation of a fluidic deflector-jet amplifier.

The strain of the GMM rod, $\varepsilon = y/L_G$, which can be written as

$$\varepsilon = \frac{\sigma}{E^H} + \lambda \tag{54}$$

where σ is the prepressure stress on the GMM rod, σ, is approximatively constant in the process of the GMM rod stretching out and drawing back. So the velocity, v, of the actuator can be written as follows:

$$v = \frac{dy}{dt} = \frac{d\varepsilon}{dt}L_G \approx \frac{d\lambda}{dt}L_G. \tag{55}$$

Substituting (55) into (53),

$$E^H A_G \lambda = m\frac{d^2y}{dt^2} + C\frac{dy}{dt} + Ky. \tag{56}$$

Equation (6) is the same as equation (50) and equation (51) in the manuscript.

Using Laplace's transforms in equation (56) yields

$$y = \frac{A_G E^H \lambda}{ms^2 + Cs + K}. \tag{57}$$

3.5. Model of deflector-jet hydraulic amplifier

A schematic representation of a deflector-jet hydraulic amplifier is shown in figure 5. Hydraulic fluid at system pressure is fed to the jet-nozzle, which directs a fine stream of fluid at two receivers. At null (no signal to the GMA), the jet stream impinges on each receiver equally, and therefore equal pressure is applied to each receiver. When an electrical input signal is applied to the coils of the GMA, an electromagnetic force is created. The force causes the GMM rod to extend in a horizontal direction, resulting in more fluid impinging on one receiver than the other. The resulting differential pressure between the two receivers is created.

Consider the deflector-jet amplifer shown in figure 6. The four variable orifices are completely analogous to the four arms of a wheatstone bridge. Arrows at the ports indicate the assumed directions of flows, and the numbers at ports refer to subscripts of the flow and the area at the ports.

Let the GMA be given a positive displacement from the null or neutral position (that is, the position $y = 0$) and the continuity equations for the two valve chambers are

$$q_L = q_1 - q_4 = C_d A_1 \sqrt{\frac{2}{\rho}(p_s - p_1)} - C_d A_4 \sqrt{\frac{2}{\rho} p_1} \tag{58}$$

$$q_L = q_3 - q_2 = C_d A_3 \sqrt{\frac{2}{\rho} p_2} - C_d A_2 \sqrt{\frac{2}{\rho}(p_s - p_2)}, \tag{59}$$

$$p_L = p_1 - p_2 \tag{60}$$

where q_L is the flow-through load and p_L is pressure drop across the load. A_1, A_2, A_3, A_4 are functions of GMA displacement:

$$A_1 = A_1(y) = A_1(0) + \beta_1 y \tag{61}$$

$$A_2 = A_2(-y) = A_2(0) - \beta_1 y \tag{62}$$

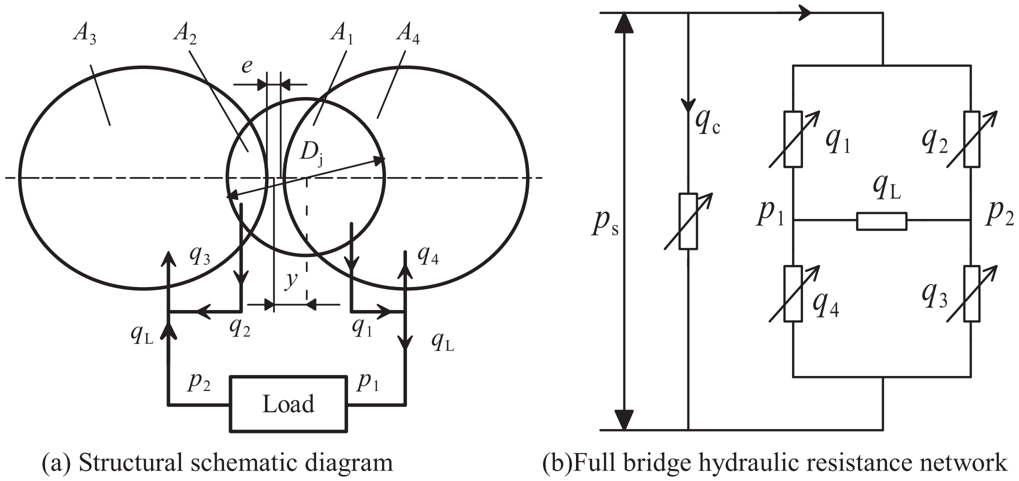

Figure 6. Full bridge hydraulic resistance network of a fluidic deflector-jet amplifier.

$$A_3 = A_3(y) = A_3(0) + \beta_2 y \tag{63}$$

$$A_4 = A_4(-y) = A_4(0) + \beta_2 y. \tag{64}$$

Consider the boundary conditions for A_1, A_4 as follows:

$$A_{1\,\min} = A_1(y)\big|_{y=0.5e-R_j} = 0 \tag{65}$$

$$A_{1\,\max} = A_1(y)\big|_{y=R_j+0.5e} = \pi R_j^2 \tag{66}$$

$$A_{4\,\max} = A_4(y)\big|_{y=0.5e-R_j} = \pi R_r^2/\cos\theta_r \tag{67}$$

$$A_{4\,\min} = A_4(y)\big|_{y=0.5e+R_j} = \pi\left(R_r^2/\cos\theta_r - R_j^2\right). \tag{68}$$

Equations (65)–(68) may be solved simultaneously to obtain

$$\begin{aligned} A_1(0) &= \frac{\pi}{2}R_j\left(R_j - 0.5e\right),\\ \beta_1 &= \frac{\pi}{2}R_j,\\ A_4(0) &= \frac{\pi R_r^2}{\cos\theta_r} + \frac{\pi}{2}R_j\left(0.5e - R_j\right),\\ \beta_2 &= \frac{\pi}{2}R_j. \end{aligned} \tag{69}$$

Substituting (69) into (61)–(64) yields

$$A_1(y) = \frac{\pi}{2}R_j\left(R_j - 0.5e + y\right) \tag{70}$$

$$A_2(y) = \frac{\pi}{2}R_j\left(R_j - 0.5e - y\right) \tag{71}$$

$$A_3(y) = \frac{\pi R_r^2}{\cos\theta_r} + \frac{\pi}{2}R_j\left(0.5e - R_j + y\right) \tag{72}$$

$$A_4(y) = \frac{\pi R_r^2}{\cos\theta_r} + \frac{\pi}{2}R_j\left(0.5e - R_j - y\right). \tag{73}$$

Thus, seven equations, (58) ~ (60), (70) ~ (73), are required to define the pressure-flow behavior of the deflector-jet amplifier. These seven equations can be solved simultaneously to yield load flow as a function of valve position and load pressure; that is,

$$q_L = q_L(y, p_L). \tag{74}$$

In making a dynamic analysis, the nonlinear algebraic equations which describe the pressure-flow curves must be linearized. We can express this function as a Taylor's series about the null or neutral position operating point, $q_L = q_L\left(0, p_L\right)$. Therefore

$$q_L = q_L\big|_{y=0} + \left.\frac{\partial q_L}{\partial y}\right|_{y=0}\Delta y + \left.\frac{\partial q_L}{\partial p_L}\right|_{y=0}\Delta p_L + \cdots \tag{75}$$

Consider the deflector-jet hydraulic amplifier operating in the vicinity of the null position; the higher-order infinitesimals are negligibly small, and we may write

$$q_L - q_L\big|_{y=0} = \Delta q_L = \left.\frac{\partial q_L}{\partial y}\right|_{y=0}\Delta y + \left.\frac{\partial q_L}{\partial p_L}\right|_{y=0}\Delta p_L. \tag{76}$$

In the null position of the deflector-jet hydraulic amplifier, consider $y = 0$, $R_j - 0.5e \approx R_j$, $0.5e - R_j \approx -R_j$, $\pi R_r^2/\cos\theta_r \approx \pi R_r^2$, and equation (69) to obtain

$$A_1(0) = A_2(0) = \frac{\pi}{2}R_j^2 \tag{77}$$

$$A_3(0) = A_4(0) = \pi R_r^2 - \frac{\pi}{2}R_j^2. \tag{78}$$

Consider $y = 0$, $q_L = 0$, and equations (58) and (59) to obtain

$$\begin{aligned} p_1 &= p_2\\ &= \frac{A_1^2(0)}{A_1^2(0) + A_4^2(0)}p_s\\ &= \frac{R_j^4}{R_j^4 + \left(2R_r^2 - R_j^2\right)^2}p_s\\ &= \frac{1}{1 + \left(2k_{rj} - 1\right)^2}p_s, \end{aligned} \tag{79}$$

where $k_{rj} = \frac{A_r}{A_j} = \frac{D_r^2}{D_j^2} = \frac{R_r^2}{R_j^2}$.

Substituting (58), (59), (77), (78), and (79) into (76) yields

$$\Delta q_L = k_{rj}\pi R_j C_d\sqrt{\frac{2}{\rho}\frac{p_s}{1 + \left(2k_{rj} - 1\right)^2}}\Delta y - C_d\pi R_j^2\frac{\left(k_{rj} - 1\right)^2 + k_{rj}^2}{2k_{rj} - 1}\sqrt{\frac{1 + \left(2k_{rj} - 1\right)^2}{2\rho p_s}}\Delta p_1 \tag{80}$$

$$\Delta q_L = k_{rj}\pi R_j C_d\sqrt{\frac{2}{\rho}\frac{p_s}{1 + \left(2k_{rj} - 1\right)^2}}\Delta y + C_d\pi R_j^2\frac{\left(k_{rj} - 1\right)^2 + k_{rj}^2}{2k_{rj} - 1}\sqrt{\frac{1 + \left(2k_{rj} - 1\right)^2}{2\rho p_s}}\Delta p_2. \tag{81}$$

Substituting (80) and (81) into (60) yields

$$\Delta q_L = K_{p0}\Delta y - K_{c0}\Delta p_L, \tag{82}$$

where $K_{p0} = k_{rj}\pi R_j C_d\sqrt{\frac{2}{\rho}\frac{p_s}{1 + \left(2k_{rj} - 1\right)^2}}$,

$K_{c0} = \frac{\pi}{2}C_d R_j^2\frac{\left(k_{rj} - 1\right)^2 + k_{rj}^2}{2k_{rj} - 1}\sqrt{\frac{1 + \left(2k_{rj} - 1\right)^2}{2\rho p_s}}$.

Substituting $\Delta p_L = 0$ into (82), the flow in no-load yields

$$q = q_L = K_{p0}y = k_{rj}\pi R_j C_d\sqrt{\frac{2}{\rho}\frac{p_s}{1 + \left(2k_{rj} - 1\right)^2}}y. \tag{83}$$

Substituting $\Delta q_L = 0$ into (82), the pressure in zero flow

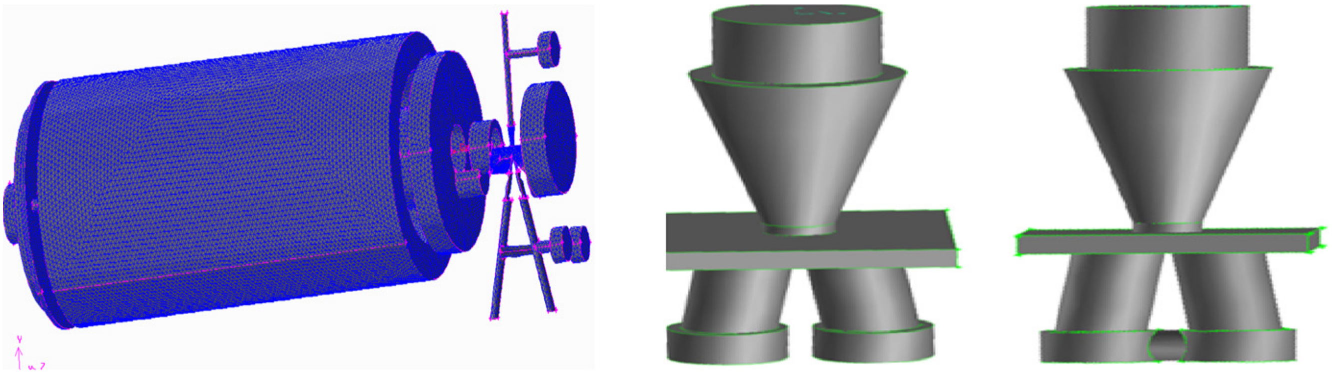

(a) The internal fluid mesh model (b) Fluid model for pressure (c) Fluid model for flow

Figure 7. The internal flow channel model of a deflector-jet servovalve driven by GMA.

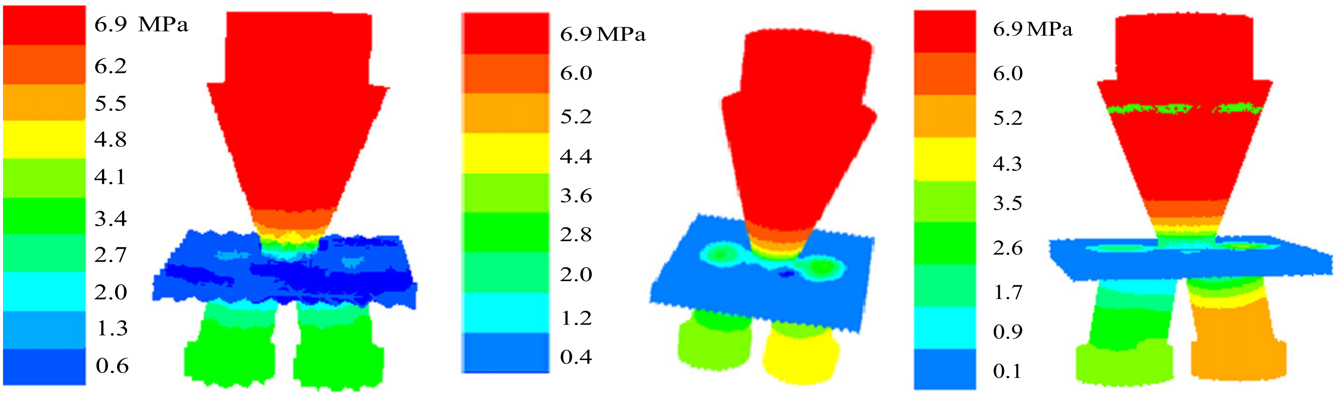

(a) y=0 (b) y=0.05 mm (c) y=0.1 mm

Figure 8. The pressure distribution of a deflector-jet servovalve driven by GMA.

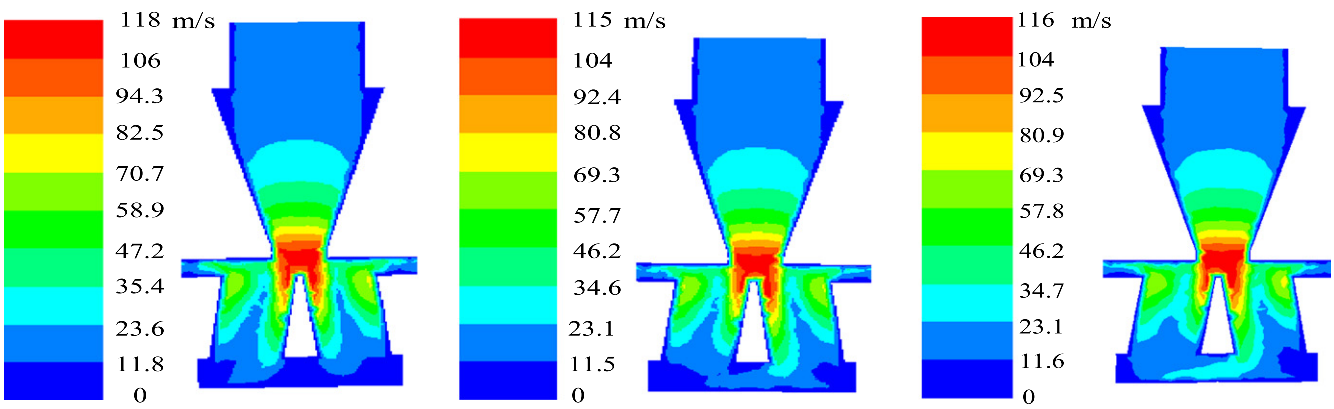

(a) y=0 (b) y=0.05 mm (c) y=0.1 mm

Figure 9. The velocity distribution of a deflector-jet servovalve driven by GMA.

yields

$$\begin{aligned} p &= p_{\mathrm{L}} \\ &= \frac{K_{\mathrm{p0}}}{K_{\mathrm{c0}}} y \\ &= K_{\mathrm{q0}} y \\ &= \frac{\pi}{2} C_{\mathrm{d}} R_{\mathrm{j}}^2 \frac{\left(k_{\mathrm{rj}} - 1\right)^2 + k_{\mathrm{rj}}^2}{2k_{\mathrm{rj}} - 1} \sqrt{\frac{1 + \left(2k_{\mathrm{rj}} - 1\right)^2}{2\rho p_s}}\, y. \end{aligned} \tag{84}$$

4. Numerical simulation

The internal flow channel model in the deflector-jet servovalve driven by GMA is built as shown in figure 7. Figures 7(b) and (c) are the numerically investigated fluid models, the blocked pressure characteristics, and the zero load flow characteristics. After accomplishing the internal flow channel model, meshing generation accordingly assumes the boundary condition as inlet pressure, $p_s = 7\mathrm{MPa}$, and outlet pressure, $p_0 = 0$.

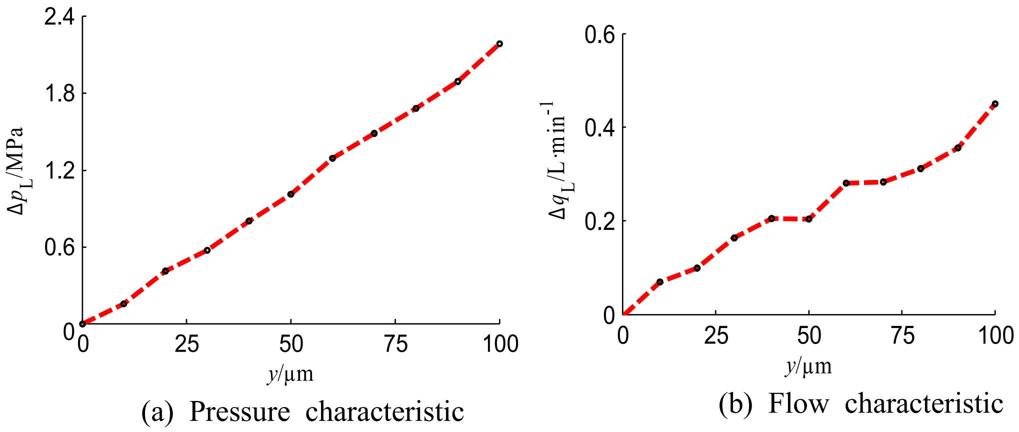

Figure 10. The simulation results of a deflector-jet servovalve driven by GMA.

The other parameters appearing in the internal flow channel model are given as density of fluid, $\rho = 850\ \mathrm{kg\ m^{-3}}$, and dynamic viscosity of fluid, $\mu_d = 0.031\ \mathrm{Pa \cdot s}$. Take the calculation model as a turbulence model. Figure 8 gives the pressure distribution results of a numerical simulation from $y = 0$, $y = 0.05$ mm, and $y = 0.1$ mm. Figure 8 shows that the pressure value is at a maximum where the fluid enters, and at a minimum at the jet-nozzle exit. The pressure value is recovered in the receiver hole. When $y = 0$, the pressure value in the two receiver holes is equal; however, when the jet-nozzle moves to the right, the pressure in the right receiver hole increases gradually, while the pressure in the left receiver hole decreases gradually.

Figure 9 gives the velocity distribution results of a numerical simulation from $y = 0$ to $y = 0.1$ mm, which show that the velocity value of the fluid in the jet-nozzle area is at a maximum. When $y = 0$, the velocity value of the fluid is zero in the middle position of the connecting pipe between the two receiver holes However, it increases gradually when the jet-nozzle moves towards the right. Figure 10 provides the numerical simulation results of a deflector-jet servovalve driven by GMA from $y = 0$ to $y = 0.1$ mm, which shows that the output pressure and output flow rate have a linear relationship with the displacement of the jet nozzle.

5. Parameter identification

First, in the above-mentioned model, the four paramenters to be identified are the eddy current loss coefficient, K_e, the hysteresis loss coefficient at intermediate fields, K_h, the Steinmetz exponent, n, and the excess loss coefficient, K_{ex}. The parameter identification method is as follows: first, based on equations (42) and (47), λ expression can be rewritten as

$$\lambda \approx K_\lambda \left[H_c(\mu' - 1 + \mu'' \tan \omega t) + M_b\right]^2 - M_b^2. \tag{85}$$

Table 2. Amplitudes of magnetic flux density, by measuring and calculating.

f(Hz)	I_m(A)	E_m(V)	B_m(T)
5	0.5	0.053	0.0300
5	0.7	0.095	0.0530
50	1.0	1.140	0.0637
100	1.0	1.900	0.0531

Substituting (57) into (85) yields

$$y = \left[\frac{Ni}{k_f L_G}(\mu' - 1 + \mu'' \tan \omega t) + M_b\right]^2 \times \frac{A_G E^H K_\lambda}{ms^2 + Cs + K} - y_b, \tag{86}$$

where y_b is the displacement generated by the bias magnetic field.

Substituting (22) into (86) yields

$$y = \left[\frac{Ni}{k_f L_G}\left(\sqrt{\left(\frac{B_m}{\mu_0 H_m}\right)^2 - \mu''^2} - 1 + \mu'' \tan \omega t\right) + M_b\right]^2 \times \frac{A_G E^H K_\lambda}{ms^2 + Cs + K} - y_b. \tag{87}$$

The voltage of the induction coil is also measured by an oscilloscope. Through measurement and calculation, the amplitudes of magnetic flux density under different alternating currents and frequencies are shown in table 2. The number of the sensing coil turns, N_c, is 150, the diameter of the induction coil, d_c, is 22 mm.

Based on equation (87) and the parameters in table 2, the output displacement, y, becomes solely a function of the imaginary part of the complex relative permeability. Due to the low permeability of the GMM rod, which has a relative permeability of less than 10, the imaginary part of the

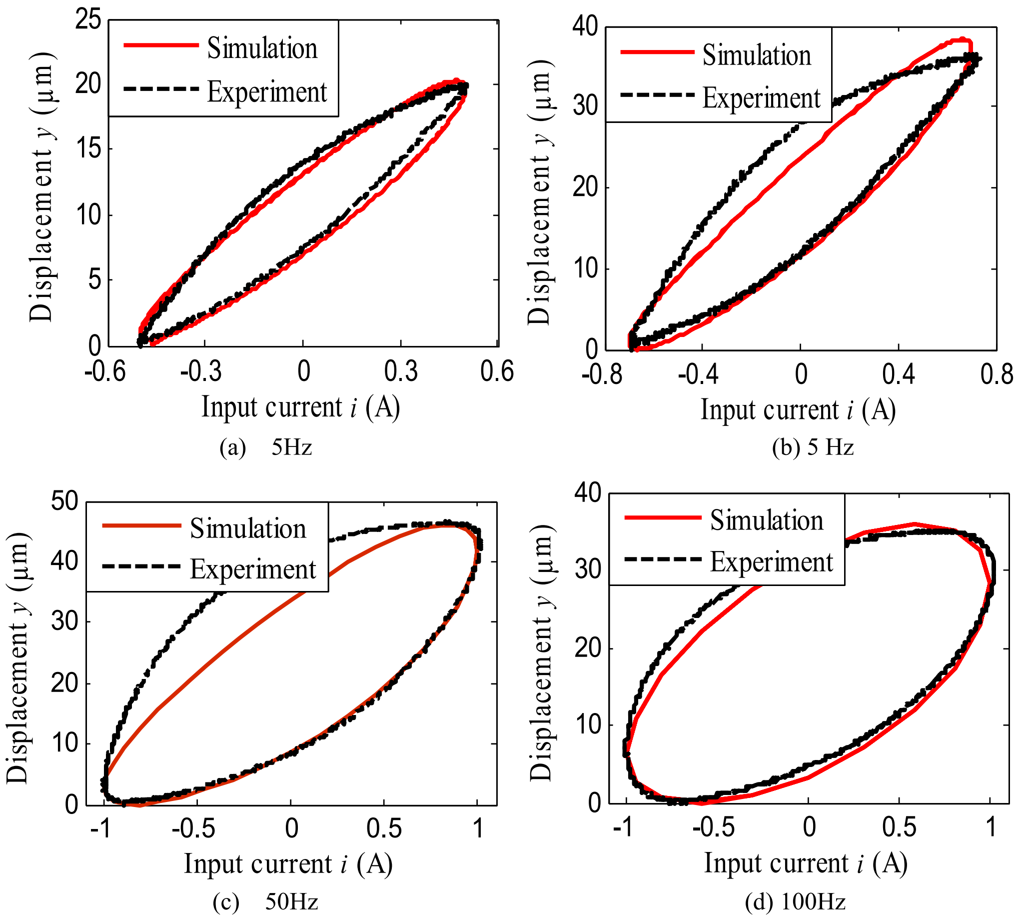

Figure 11. Output displacement versus input current used for parameter identification.

complex relative permeability can be obtained by varying its value from 0 to 10 to minimize the sum of the squares of the errors between the experiment values and the fitted values provided by equation (87). Substituting the obtained values into equation (14) can result in a set of equations; the hysteresis loss coefficient, the eddy current loss coefficient, and the anomalous loss can be identified by solving these equations. The experiment curves used for parameter identification and the simulation curves provided by equation (87) are shown in figure 11. The values of the parameters to be identified are shown in table 3.

Also, in the magnetization model of the GMM rod, the output displacement of the GMA meets equation (49), and only the imaginary part of the relative complex permeability, μ'', need be identified.

Because the lag angle caused by hysteresis increases with the amplitude value of the applied magnetic field, the value of the imaginary part of the relative complex permeability has a positive correlation with the amplitude value of the input current, so we assume

$$\mu'' = k_{\mathrm{i}} I_{\mathrm{m}}, \tag{88}$$

where k_{i} is the parameter to be identified and I_{m} is the amplitude value of the input current.

Take the amplitude value of the input current, $I_{\mathrm{m}} = 0.5$ A, and the frequency of the input current, $f = 1$ Hz. We make the

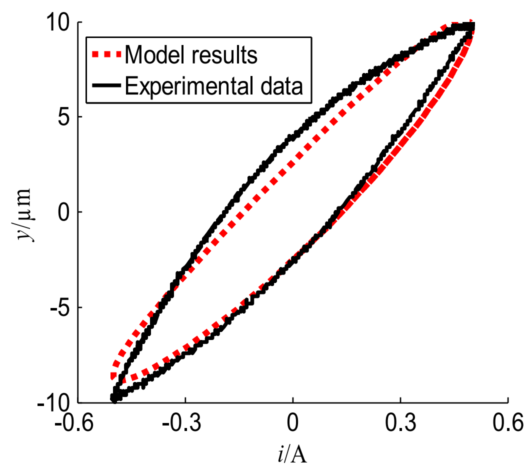

Figure 12. Identification of imaginary part for relative complex permeability.

Table 3. The value of parameters to be identified.

Parameters	Value
Hysteresis loss coefficient (K_{h})	85 805
Hysteresis loss coefficient (n)	1.8092
Eddy current loss coefficient (K_{e})	2753.39
Anomalous loss coefficient (K_{ex})	895.80

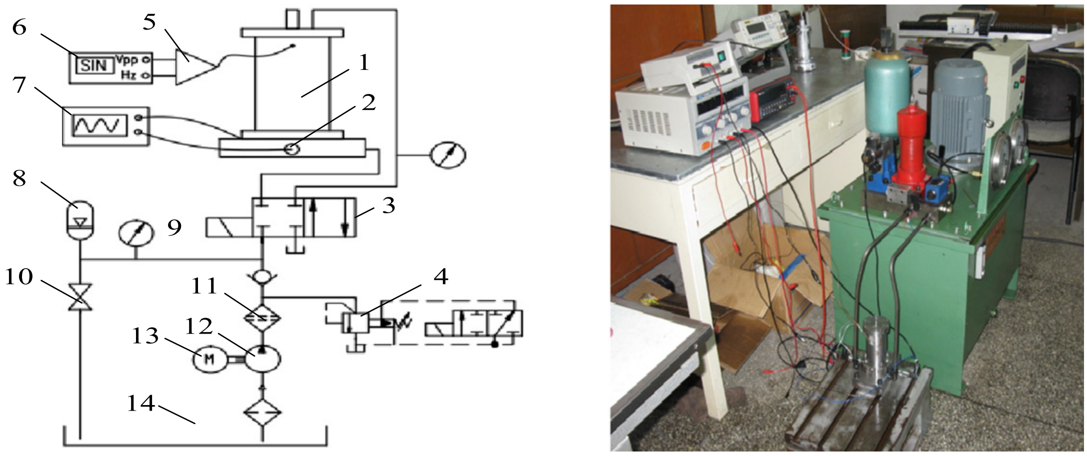

1. GMM-based DJSV 2.Pressure sensor 3. Directional valve 4. Electromagnetic relief valve 5. Power amplifier 6. Signal generator7.Oscilloscope 8. Energy accumulator9. Pressure gage 10. Stop valve 11.Fine filter 12.Pump 13.Motor 14.Tank

(a) Schematic of the servovalve experimental set-up (b) Photograph of the servovalve experimental set-up

Figure 13. Schematic diagram of the GMM-based DJSV test system.

minimum square sum of the difference value between the simulation curves and the test curves, which is shown in figure 12. Thus, we acquire the imaginary part of relative complex permeability as $k_i = 2.2$.

6. Model validation

A prototype was built and tested. The experimental results were compared with the mathematical models. The pressure response of the valve with varying drive currents was analyzed. Figure 13 shows the experiment platform used for measuring the performance of a deflector-jet electrohydraulic servovalve driven by a GMA; it consists of driving subsystems, test subsystems, and oil source subsystems.

The driving subsystem includes a signal generator and a constant-current power amplifier. The test subsystem includes a pressure sensor, pressure gauge, and an oscilloscope. The oil source subsystem includes a hydraulic pump, an electromagnetic relief valve, and a solenoid directional valve. Additional structural parameters for the deflector-jet electrohydraulic servovalve are shown in table 4.

The two receiver ports in the deflector-jet servovalve were connected to the identical pressure sensor (M5100, measuring range $0 \sim 10$ MPa, accuracy: $\pm 0.25\%$ BSL, max (combined linearity, hysteresis, andrepeatability)). The test fluid used was HM-32 mineral oil. A schematic and photograph of the valve test rig are shown in figures 13(a) and (b), respectively. The experiment operates as follows.

Step 1: First, the oil pressure of the hydraulic pump exit port is set by an electromagnetic relief valve, which supplies oil to the jet-nozzle with a solenoid directional valve. Accumulators were used at the supply and return ports of the valve to provide near constant pressure.

Step 2: At the null position (no voltage to the drive coil of the GMA), the flow from the deflector impinges equally on the two receiver ports, so that the pressures on the two receiver exit ports are equal.

Table 4. Model parameters for the GMA.

Parameters	Value
Radius of GMM rod (r_G) [mm]	5
Length of GMM rod (L_G) [mm]	80
Equivalent mass of GMA (m) [kg]	0.1
Equivalent damping of GMA (c) [Ns m^{-1}]	3000
Equivalent stiffness of GMA (K) [N m^{-1}]	9.9×10^6
Bias magnetization (M_b) [kA m^{-1}]	160
Leakage coefficient of the magnetic flux (K_f)	1.2
Number of the excitation coil (N) [turns]	1300
Young modulus of GMM rod (E^H) [GPa]	20
Electrical resistivity of GMM rod (ρ) [Ωm]	6×10^{-7}
Inductance of drive coil (L) [mH]	6
Resistance of drive coil (R) [Ω]	6
Sampling resistance (R_0) [Ω]	0.5

Step 3: When a voltage from the signal generator is applied to the power amplifier, which converts and magnifies it as a current signal, the control magnetic field is established immediately, so the actuator moves the deflector.

Step 4: The displacement of the deflector differentially directs the jet of fluid toward one of the two receiver ports, thus increasing the pressure in that port. This phenomenon creates a pressure imbalance between the two receivers. Accordingly, differential pressure is built between the two receivers.

6.1. Static characteristics

The static characteristics are the relationship between the output pressure and the input current under rated supply pressure, which is obtained by the quasi-static harmonic input current. The rated supply pressure is 7 MPa, the amplitude of the input current is 1 A (from −0.5 A to 0.5 A) and 2 A

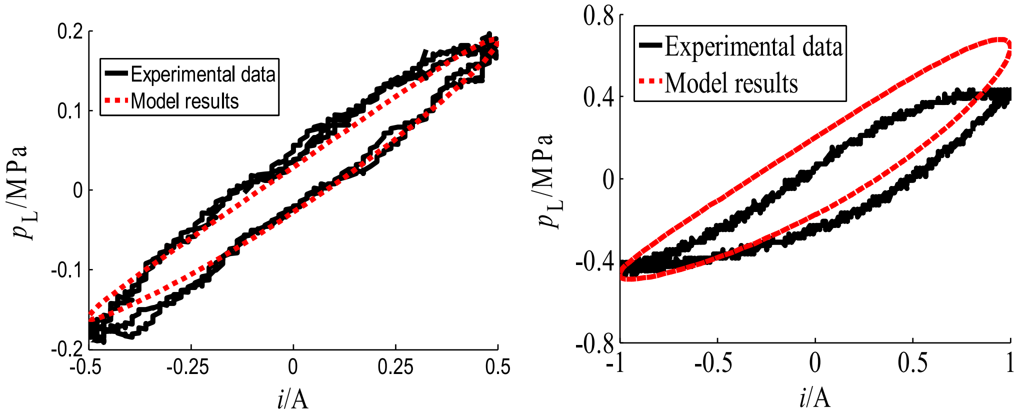

(a) Input current from -0.5A to 0.5A (b) Input current from -1A to 1A

Figure 14. Output pressure generated by the input current at static in a GMM-based DJSV.

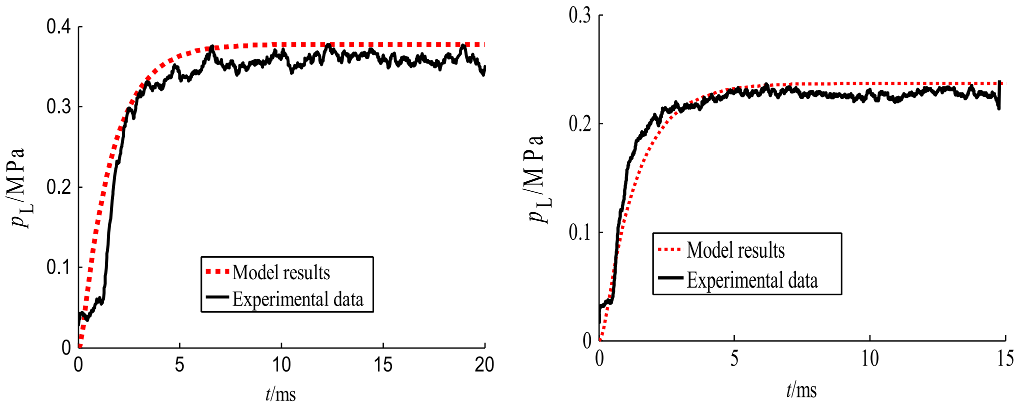

(a) Step input current from 0 to 1A (b) Step input current from 0 to 0.5A

Figure 15. Output pressure generated by step input current in a GMM-based DJSV.

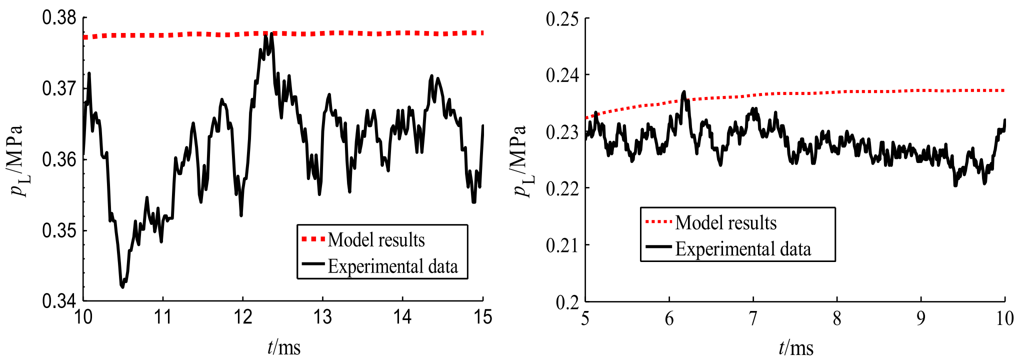

(a) Step input current from 0 to 1A (b) Step input current from 0 to 0.5A

Figure 16. Steady-state output pressure generated by step input current in a GMM-based DJSV.

(from −1 A to 1 A), and the frequency of the input current is 0.1 Hz.

Figure 14 shows the model calculation results and the experimental data of the static output pressure for the deflector-jet electrohydraulic servovalve driven by a GMA. When the input current varies from −0.5 A to 0.5 A, the output pressure has a variation range from −0.18 MPa to 0.19 MPa, and the model results and the experimental data have a good agreement, as shown in figure 14(a).

However, when the input current varies from −1 A to 1 A, based on the experimental data, the output pressure changes from −0.47 MPa ~ 0.45 MPa, and the model results overestimate the value of the output pressure, which is shown in figure 14(b).

By comparing the hysteresis loop in figures 14(a) and (b) with the increase of the input current amplitude, it is observed that the output pressure hysteresis loop varies from a symmetrical loop to an asymmetrical loop. Thus, the nonlinear characteristics of the output pressure become more serious,

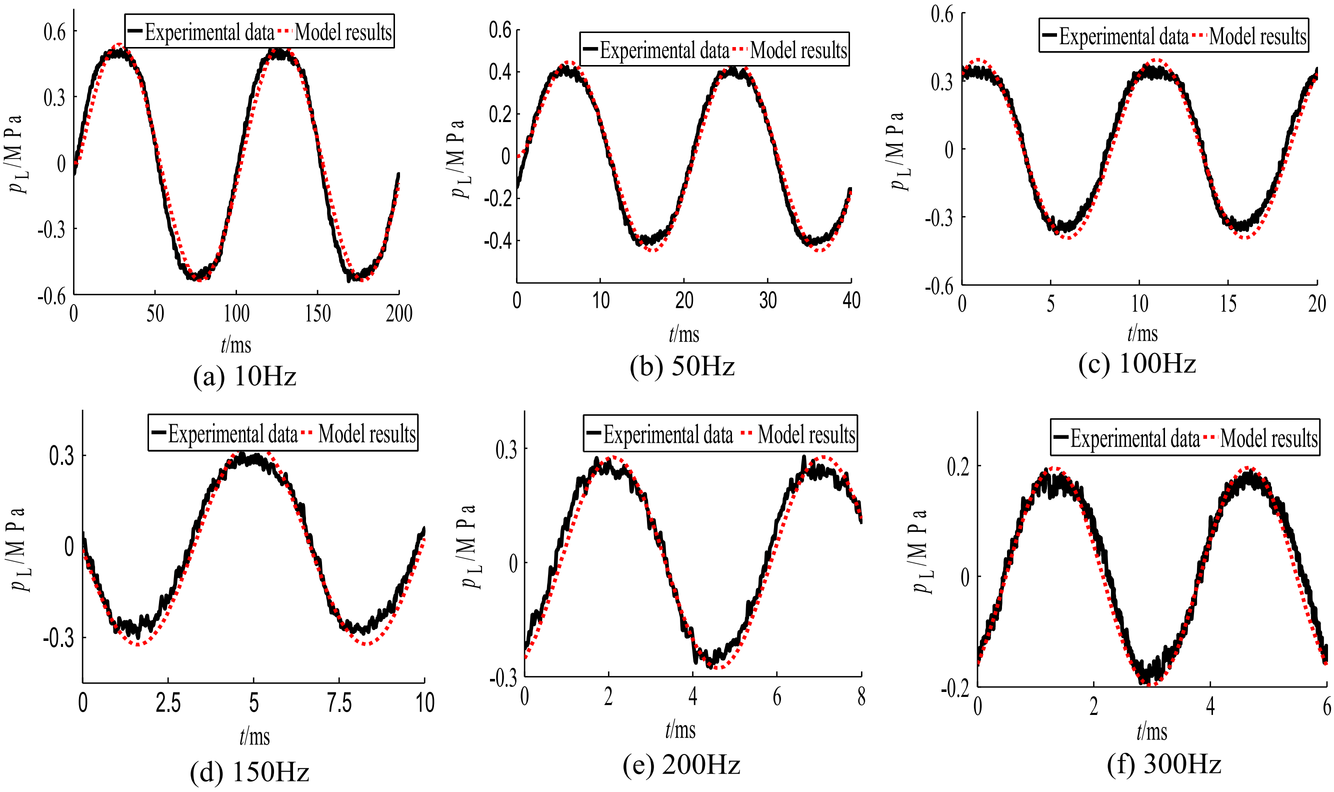

Figure 17. Sinusoidal response curves of a GMM-based DJSV.

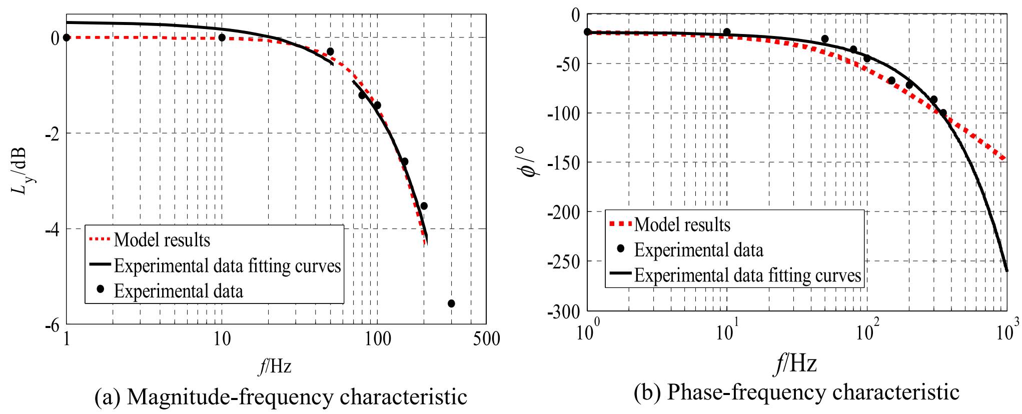

Figure 18. Frequency characteristic of the GMM-based DJSV.

which indicates that the maximum input current of this servovalve is limited, and hysteresis inverse compensation measures should be taken under the large input current in the deflector-jet electrohydraulic servovalve driven by a GMA.

6.2. Step response

The time response of the deflector-jet electrohydraulic servovalve driven by the GMA was carried out with step input. The time response was evaluated using the setup, as shown in figure 13. The valves were commanded by a step voltage, and then the pressure was recorded using an oscilloscope. The recorded data were subsequently analyzed in a computer and the curves were plotted as shown in figure 15. As figure 15(a) shows, the time required to reach the steady-state output pressure for a step input signal is approximate 3 ms. As figure 15(b) indicates, the steady-state output pressure value will reach 0.23 MPa and 0.37 MPa for the step input current from 0 to 1 A and the step input current from 0 to 0.5 A, respectively.

From the model results and experimental data in figure 15, we can see that this servovalve can obtain fast transition properties without ripple or overadjustment. Moreover, the above-mentioned model prediction results for this servovalve coincide perfectly with the experimental results. From the model results and experimental data in figure 16, the steady-state output pressure of the prototype valve is in good agreement with the predicted results.

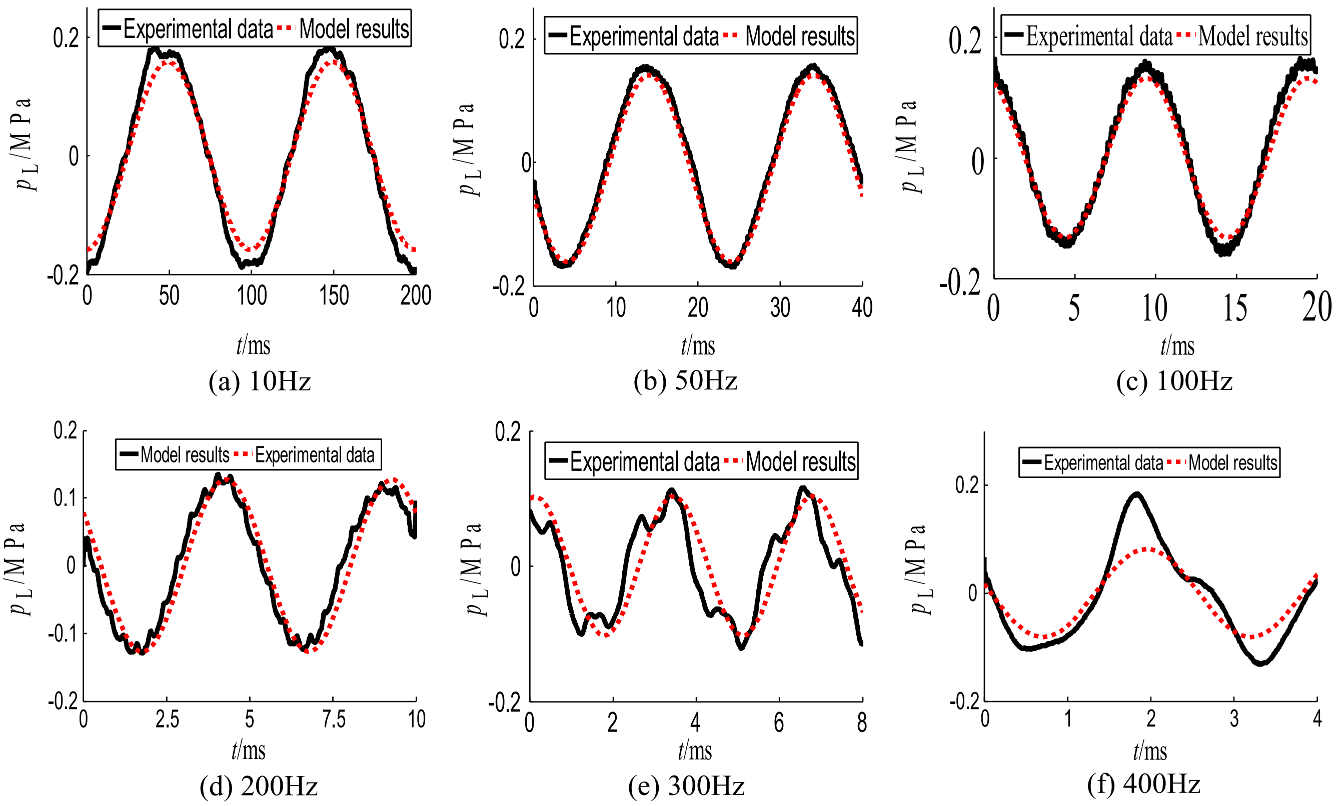

Figure 19. Sinusoidal response curves of a GMM-based DJSV.

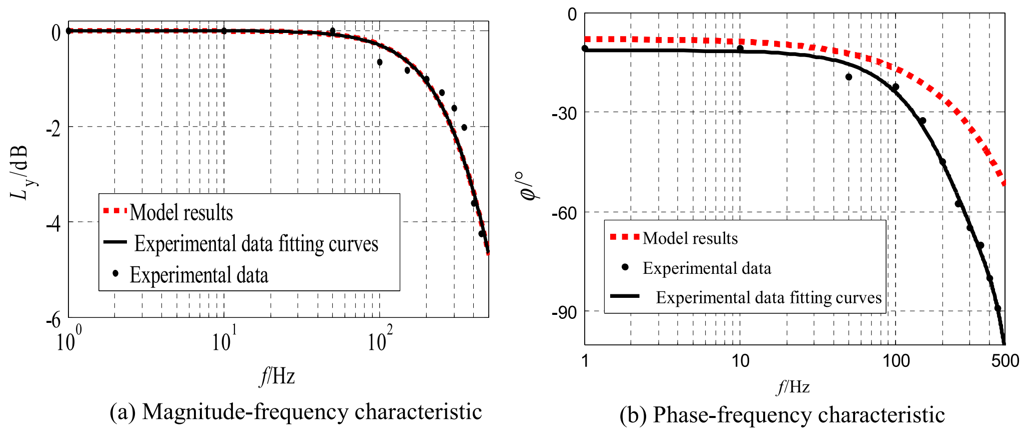

Figure 20. Frequency characteristics of a GMM-based DJSV.

6.3. Sinusoidal response and frequency characteristics

The pressure response of the two receiver ports with sinusoidal supply voltages is analyzed. The operating conditions supply pressure of 7 MPa and an exciting coil voltage amplitude of 2 V (corresponding to current 1 A). The test setup is shown in figure 13. The operating process is as follows.

First, adjust the jet nozzle (the output rod of the GMA) to the null position. Next, supply sinusoidal voltage from a signal generator to the power amplifier; the voltage frequency varies from 10 Hz to 300 Hz. The pressure response curve is captured by an oscilloscope, and the corresponding data are recorded and plotted in figure 17 with model simulation data. Figure 17 shows reasonable agreement between the experimental data and the model results.

Based on the results in figure 17, the output pressure magnitude-frequency characteristic and phase-frequency characteristic of the deflector-jet electrohydraulic servovalve driven by a GMA are plotted in figure 18. As figure 18(a) shows, under 1 A input current amplitude, the −3 dB bandwidth from the experimental data and the model results is approximately 150 Hz, and the theoretical results are in perfect agreement with the experimental data. As figure 18(b) shows, under 1 A input current amplitude, the −90° phase bandwidth from the experimental data and the model results is

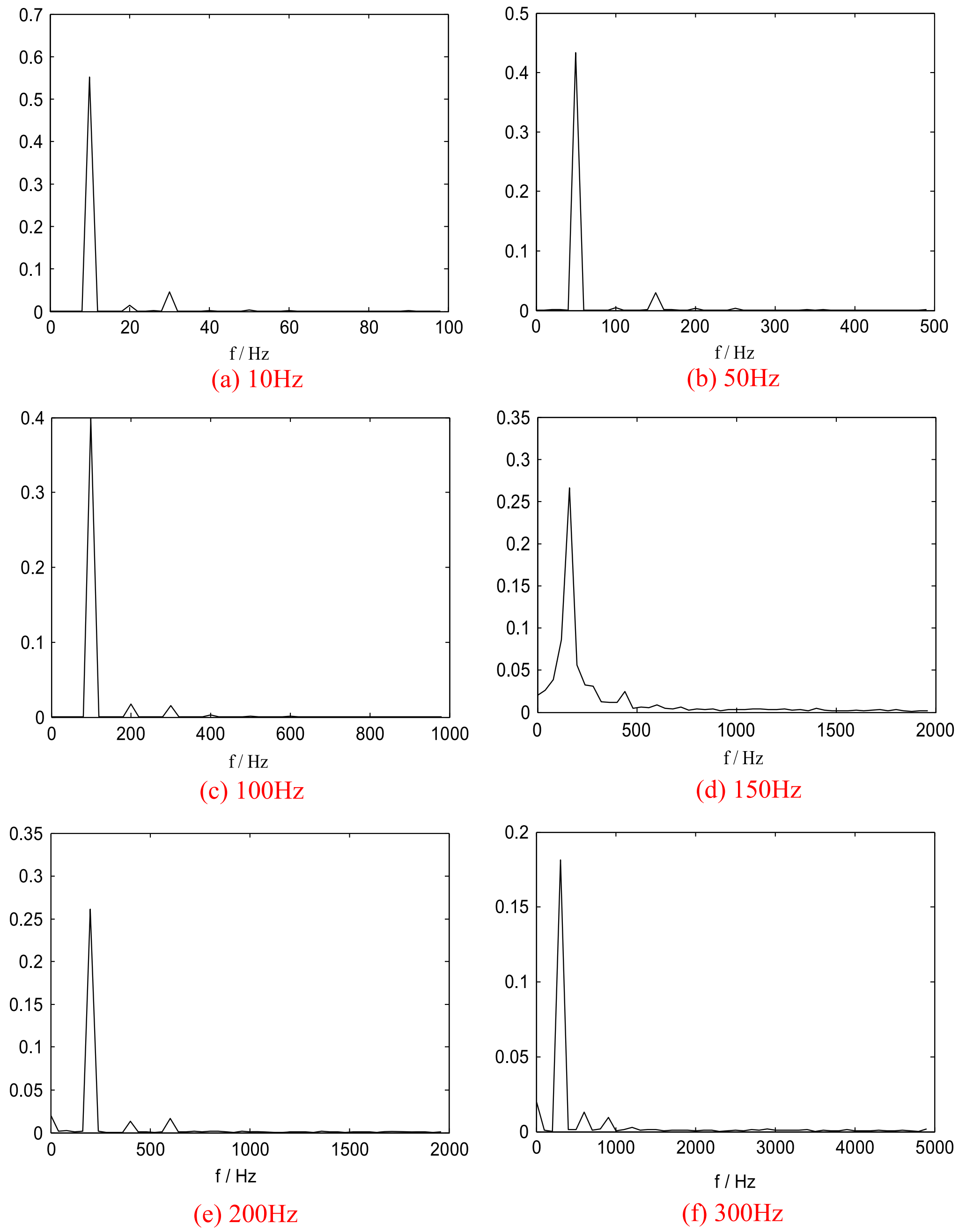

Figure 21. Spectral analysis results with input current 1 A and an excitation frequency from 10 Hz to 300 Hz.

approximately 300 Hz, and the experimental data are slower than those of the model predictions.

The following part is the pressure response of the two receiver ports with a sinusoidal supply voltage amplitude of 1 V (corresponding current: 0.5 A). The voltage frequency varies from 10 Hz to 400 Hz. The other operating conditions are the same as for the part outlined above. Figure 19 gives the sinusoidal pressure-response curves for both the experimental data and the model results.

Based on the results in figure 19, the output pressure magnitude-frequency characteristic and phase-frequency characteristic of deflector-jet electrohydraulic servovalve driven by GMA are plotted in figure 20. As figure 20(a) shows, under the 0.5 A input current amplitude, the −3 dB bandwidth from the experimental data and the model results is approximately 350 Hz, and the theoretical results of output pressure magnitude bandwidth agree perfectly with the experimental data. As figure 20(b) shows, under the 0.5 A input current amplitude, the −90° phase bandwidth from the experimental data and the model results is approximately 500 Hz, and the experimental data are slower than the model predictions as well.

Moreover, as shown in figures 14–17, and 19, the actual measured pressure data exhibit significant ripples. With the goal of uncovering the nature hidden behind the experimental curve, a spectral analysis with input current 1 A and excitation frequency from 10 Hz to 300 Hz was completed. The results of this analysis are shown in figure 21, proving the prediction that random noise is what excites the ripples in the experimental curve.

7. Summary and conclusions

(1) In this paper, a new type of GMM-based DJSV is developed for the first time, which is mechanically less complex than the conventional torque motor and avoids the use of a torque motor that requires manual assembly and careful air-gap adjustment; hence, its reliability is higher than the conventional servovalve.
(2) In the present study, the model of a GMM-based DJSV is built, which involves five submodels from the viewpoint of energy conversion and incorporates both the frequency-dependent hysteresis and the magnetomechanical behaviors of the magnetostrictive actuator; the model results indicate that it can describe the relation between the applied field and the output pressure for the servovalve over a broad range of operating conditions, which is of great practical value in estimating and controlling the new type of servovalve.
(3) The blocked pressure characteristics and zero-load flow characteristics of the GMM-based DJSV are numerically investigated based on computational fluid dynamics models established in this article, which show that the output pressure and output flow rate have a good linear relation with the displacement of the jet nozzle.
(4) The system model parameters are in some cases estimated from physical design data and are also derived or verified by experimental data. The match between the simulated and experimental results indicates that the behavior of the servovalve is largely understood.
(5) The experiment platform used for measuring the performance of a GMM-based DJSV is also established, a simulation and experimental research on the servovalve are performed, and the results demonstrate that the present GMM-based DJSVs have a large output pressure range, rapid response, and high bandwidth, which provide a competitive way to develop a new type of high-frequency and high-flow-rate electrohydraulic servovalve.

Acknowledgments

This work was supported by the National Natural Science Foundation of China [grant number 51175243]; the Natural Science Foundation of Jiangsu Province [BK20131359]; and the Aeronautical Science Foundation of China [grant number 20130652011].

References

Sangiah D K, Plummer A R, Bowen C R and Guerrier P 2013 A novel piezohydraulic aerospace servovalve. part 1: design and modelling *Proc. Inst. Mech. Eng. Journal of Systems and Control Engineering* **227** 371–89
Ding F *et al* 2002 The study of pneumatic servo valve and inchworm based on GMM *Journal of China Coal Society.* **27** 440–3
Engdahl G 1999 *Handbook of Giant Magnetostrictive Materials* (San Diego: Academic)
Braghin F, Cinquemani S and Resta F 2012 A low frequency magnetostrictive inertial actuator for vibration control *Sensors and Actuators A: Physical* **180** 67–74
Grunwald A and Olabi A G 2008 Design of a magnetostrictive (MS) actuator *Sensors and Actuators A: Physical* **144** 161–75
Hiratsuka K and Urai T 1994 Magnetic circuit design of a giant magnetostrictive actuator and application to a direct-drive servo valve *Japan Society of Mechanical Engineers* **60** 479–83
Jiles D C 1994 Modelling the effects of eddy current losses on frequency dependent hysteresis in electrically conducting media *IEEE Trans. Magn.* **30** 4326–8
Karunanidhi S and Sigaperumal M 2010 Design, analysis and simulation of magnetostrictive actuator and its application to high dynamic servo valve *Sensors and Actuators A: Physical* **157** 185–97
Li Y S, Zhu Y C and Wu H T 2011a Parameter optimization of jet-pipe servovalve driven by giant magnetostrictive actuator *Acta Aeronautica et Astronautica Sinica* **32** 1336–44
Li Y S and Zhu Y C 2012b Research on displacement-sensing model and hysteresis loop of giant magnetostrictive actuator *J. Mech. Eng.* **48** 169–74
McCloy D and Martin H R 1980 *Control of Fluid Power Analysis and Design* (Chichester: Ellis Horwood/JohnWiley)
Merrit H E 1967 *Hydraulic Control Systems* (New York: John Wiley)
Olabi A G and Grunwald A 2008 Design and application of magnetostrictive materials *Mater. Des.* **29** 469–83
Pradhan S C 2005 Vibration suppression of FGM shells using embedded magnetostrictive layers *Int. J. Solids Struct.* **42** 2465–88
Shang X C, Pan E and Qin L P 2008 Mathematical modeling and numerical computation for the vibration of a magnetostrictive actuator *Smart Mater. Struct.* **17** 045026
Karunanidhi S and Singaperumal M 2010 Design, analysis and simulation of magnetostrictive actuator and its application to high dynamic servo valve *Sensors and Actuators.* A **157** 185–97
Sun L and Zheng X J 2006 Numerical simulation on coupling behavior of terfenol-D rods *Int. J. Solids Struct.* **43** 1613–23
Urai T and Tanaka H 2001 Development of a giant magnetostrictve tandem actuator and application to a servovalve *Nihon Yukuatsu Gakkai Ronbunshu* **32** 53–7
Tan X and Baras J S 2004 Modeling and control of hysteresis in magnetostrictive actuators *Automatica* **40** 1469–80
Urai T 1995 Development of a giant magnetostrictive actuator with stroke expansion system and application to a servo valve *The Japan Society Applied to Electromagnetics and Mechanics* **3** 46–9
Valadkhan S, Morris K and Shum A 2010 A new load-dependent hysteresis model for magnetostrictive materials *Smart Mater. Struct.* **19** 125003
Wang C L, Ding F and Fang P 2005 Control pressure characteristics of nozzle flapper valve based on GMA *Chin. J. Mech. Eng.* **41** 127–30
Wang C L, Ding F and Cui J 2006 Dynamic characteristics of nozzle flapper servo valve based on GMA *Chin. J. Mech. Eng.* **42** 23–6
Wang C L, Ding F and Li Q P 2007 Study on driving magnetic field and performance of GMA for nozzle flapper servo valve *Journal of Coal Science & Engineering.* **13** 207–10
Wang X, Wang S and Liu J 2009 Research on a new type of sea water hydraulic servovalve driven by diphase oppositing giant magnetostrictive self-sensing actuator[C] *2009 Int. Conf. on Measuring Technology and Mechatronics Automation (ICMTMA 2009) (Zhangjiajie,Hunan, China) IEEE Computer Society*, Vol 1, April 11~12: 109~11

Wang X, Ya Q and Wang D 2010 Research on double outputs high-precision digital control stabile voltage power for diphase opposition giant magnetostrictive self-sensing actuator *Int. Conf. on Measuring Technology and Mechatronics. Automation* pp 53–6

Watton J 1989 *Fluid Power Systems: Modeling, Simulation, Analog and Microcomputer Control* (Hemel Hempstead, UK: Prentice-Hall)

Zheng J J, Cao S Y, Wang H L and Huang W W 2007 Hybrid genetic algorithms for parameter identification of a hysteresis model of magnetostrictive actuators *Neurocomputing* **70** 749–61

Zhou H M, Zheng X J and Zhou Y H 2006 Active vibration control of nonlinear giant magnetostrictive actuators *Smart Mater. Struct.* **15** 792–8